Electrochimica Acta 548 (2026) 147979

Contents lists available at ScienceDirect

Electrochimica Acta

journal homepage: www.journals.elsevier.com/electrochimica-acta

Beyond pure precursors: Towards oxygen reduction reaction activity enhancement in PEM fuel cells from recycled mining waste

Diana Orozco-Gallo [a,*], Ricardo Ossa-Gallego [a], Catalina Orozco-Silva [a], Verónica Muñoz-Montes [a], Soufiane Boudjelida [b], Gioele Pagot [b], Enrico Negro [b], Vito Di Noto [b], Jorge A. Calderón [a,*]

[a] Centro de Investigación, Innovación y Desarrollo de Materiales – CIDEMAT. Universidad de Antioquia., Street 70 N# 52 – 21, Medellín, Colombia
[b] Section of "Chemistry for the Technology" (ChemTech), Department of Industrial Engineering, University of Padova, Via Marzolo 9, I-35131, Padova, PD, Italy

ARTICLE INFO

Keywords:
PEM fuel cells
Oxygen reduction reaction
Pt/C
Recycled mining precursors
Statistical design of experiments

ABSTRACT

Clean energy is essential to achieving the United Nations' Sustainable Development Goals and targets. Proton Exchange Membrane Fuel Cells (PEMFCs) are one of the leading technologies for implementing the "hydrogen economy" and contributing to a sustainable energy supply. PEMFC development requires high-performing, durable electrocatalysts (ECs) whose synthesis is as facile and inexpensive as possible. This work demonstrates that it is feasible to synthesize viable ECs for PEMFCs from platinum mining residues obtained in Colombia. This Pt source is hardly exploited and, in perspective, could offer a lower-cost alternative to more established precursors for the preparation of ECs for PEMFCs. In particular, the ECs considered in this work are intended to promote the oxygen reduction reaction (ORR), a key bottleneck in PEMFC operation. The precursors from mining residues were characterized by micro-Raman, ATR-FTIR, XRD, TGA, and SEM/EDS to clarify their chemical composition and identify the coordination complexes present therein. Two synthetic methods are considered: (i) the micro-emulsion method; and (ii) the polyol method. A statistical Design of Experiments (DoE) is implemented to determine the optimal experimental conditions for each synthetic method. The physicochemical properties of the resulting Pt/C ECs are elucidated by SEM, TEM/STEM-EDS, XRD, and XPS. Finally, it is found that the *"ex-situ"* ORR performance determined by the CV-TF-RRDE method of the Pt/C ECs presented in this work compares favorably to that of a state-of-the-art Pt/C EC benchmark for the ORR.

1. Introduction

Energy transition targets associated with the Paris Agreement towards a decrease in pollution and a mitigation of the greenhouse effect have put the *"hydrogen economy"* (where fuel cells play a key role) in the spotlight [1,2] In the last decades, platinum has been increasingly used in the development of clean energy technologies. In particular, platinum is used in catalytic converters for automotive applications [3]. Consequently, as of today almost 60 % of the total platinum demand comes from the automotive sector. Platinum also plays a crucial role in the promotion of electrochemical processes based on the operation of proton exchange membrane fuel cells (PEMFCs), with a particular reference to the oxygen reduction reaction (ORR) taking place at the cathode. Indeed, this latter process exhibits sluggish kinetics if compared with the hydrogen oxidation reaction (HOR) occurring at the anode [4–6]. In a typical 80 kW stack for automotive applications, the cost of the electrodes as driven by the Pt content is expected to account for more than half of the overall cost. Hence, finding new platinum sources to diversify the supply and curtail losses is significant [7].

Platinum (Pt) and other platinum group metals (PGMs) like Ir, Pd, Ru, and Rh are scarce in Earth's crust, with Pt concentrations around 0.4 ppb. While South Africa and Russia dominate global reserves, Colombia holds smaller deposits in komatiite and associated mafic rocks, with Pt concentrations up to 25 ppb [8]. Extracting Pt in Colombia faces significant challenges due to the low concentration and high impurity of local sources, making the production of viable Pt precursors economically demanding [9,10]. Recovery from mining residues is emerging as a promising alternative, with companies like the Altea Group working to

* Corresponding authors.
E-mail addresses: dcorozcog@unal.edu.co (D. Orozco-Gallo), soufiane.boudjelida@studenti.unipd.it (S. Boudjelida), gioele.pagot@unipd.it (G. Pagot), enrico.negro@unipd.it (E. Negro), vito.dinoto@unipd.it (V. Di Noto), andres.calderon@udea.edu.co (J.A. Calderón).

https://doi.org/10.1016/j.electacta.2025.147979
Received 3 December 2025; Accepted 7 December 2025
Available online 7 December 2025

recycle these materials into PGM complexes for application as precursors to synthesize electrocatalysts for PEM fuel cells. Despite high purification costs and low recovery yields, this approach could diversify global Pt supply, reduce dependence on traditional sources, and create new revenue streams for Colombia's mining sector. By starting from secondary raw materials including impure PGMs it could still be possible to obtain viable ECs without the need to resort to commercial PGM precursors obtained from a small number of traditional suppliers [11, 12].

Recycling platinum group metals (PGMs) offers a sustainable route for electrocatalyst synthesis, with increasing evidence supporting the use of recycled precursors in fuel cell technologies. Despite the presence of impurities such as transition metals, sulfur, and organics, which can affect the activity and the durability of the electrocatalyst, recovery methods like hydrometallurgical and electrochemical processes have shown promise in improving extraction yields and precursor purity [13–15]. Strategies to mitigate impurity effects include chemical treatments, purification protocols, and impurity-tolerant catalyst designs that reduce processing complexity and cost [16–18].

Moreover, hydrophobic deep eutectic solvents (DESs), such as trihexyl(tetradecyl)phosphonium chloride combined with decanoic acid, have demonstrated selective leaching of Pt, Pd, and Rh from spent automotive catalysts, achieving up to 90 % Pt recovery while minimizing co-leaching of base metals [19]. Similarly, solvometallurgical methods using $FeCl_3$ in acetonitrile offer selective Pt recovery with reduced environmental impact and closed-loop solvent regeneration [20]. From PEMFC membrane electrode assemblies (MEAs), chlorine-based hydrometallurgy has enabled >99 % Pt recovery. The resulting impure Pt precursor was directly reused to synthesize Pt/C electrocatalysts, which exhibited oxygen reduction reaction (ORR) mass activity of 170 mA/mg_{Pt}, comparable to a commercial Pt/C benchmarks.

Electrochemical and structural analyses confirm that a low level of impurities can be effectively managed through optimized synthesis and support selection, enabling efficient operation in fuel cell environments [13,14]. Long-term testing under realistic cycling conditions shows that recycled PGM electrocatalysts maintain stable power outputs and resist common degradation pathways [17,21]. These developments align with circular hydrogen economy principles by minimizing resource consumption and processing steps [13].

The methodology presented here for tuning synthesis parameters enables the direct use of low-purity precursors to produce viable Pt/C ECs for the ORR starting from PGM precursors obtained in Colombia in the perspective of diversifying the Pt supply and reducing the costs of PEMFC electrodes with mass activities and ECSA comparable to benchmark materials, highlighting the practical viability of PGMs obtained from non-conventional sources (*i.e.*, neither primary ores nor conventional secondary sources such as automobile catalytic converters and used MEAs) in fuel cell applications. The Pt/C ECs are obtained by optimizing the synthetic parameters of well-assessed bottom-up preparation routes. The polyol and microemulsion [22,23] methods are low-cost, environmentally friendly techniques to synthesize Pt nanoparticles. The polyol method allows precise control over nanoparticle features by adjusting medium composition, pH, temperature, reaction time, precursor chemistry, and additives [24,25]. The microemulsion method, while similarly mild and straightforward, requires stable emulsions influenced by precursor concentration, surfactants, temperature, and sample purity [22,23]. A key challenge in both methods is the use of impure precursors, such as those derived from mining residues which can destabilize microemulsions and complicate synthesis. Despite these limitations, this work shows that both methods remain viable for producing metal-based nanoparticles without requiring high-temperature conditions.

The preparation of Pt nanoparticles suitable for ORR ECs is possible only by reducing the PGM complexes included in the precursors. During this process, the impurities present in the non-analytical grade precursors from mining residues might lead to undesirable co-precipitation phenomena. In addition, it is crucial to closely monitor the synthetic processes/parameters to prevent that the impurities give rise to the formation of agglomerated nanoparticles or nanostructures exhibiting undesired shapes and preferred crystal orientations [26]. On these bases, the primary goal of this work is to develop the methodology to prepare viable Pt/C ECs for the ORR starting from three non-analytical grade precursors obtained in Colombia by Altea Group from residuals of Pt and Au mining. Such precursors are characterized by micro-Raman, ATR FT-IR, XRD, TGA and SEM/EDS. Afterwards, two synthesis methods to yield the Pt/C ECs for the ORR are optimized by modulating: (i) the concentration of the precursors and the percentage of the aqueous phase in the case of the microemulsion method; and (ii) the temperature, dwell time and surfactant/precursor ratio in the case of the polyol method. The resulting Pt/C ECs for the ORR are characterized by SEM, TEM/STEM-EDS, XRD, XPS and CV-TF-RRDE and their viability is gauged *versus* a state-of-the-art Pt/C commercial EC, which is used as the benchmark.

2. Experimental

2.1. Characterization of the precursors

The vibrational features of the precursors are evaluated using a Thermo Scientific DXR micro-Raman equipped with a 532 nm laser. The micro-Raman spectra are collected at a laser power of 2 mW and with 80 acquisitions, each with 15 s of exposure. A Perkin-Elmer Spectrum Two spectrometer is used with the universal attenuated total reflectance accessory (UATR) for functional group identification. ATR FT-IR spectra are recorded within the 4000–400 cm^{-1} wavenumber interval.

Thermogravimetric analysis (TGA) is carried out on a TA instruments model Q500 equipment with nitrogen/inert atmosphere at 30 mL/min gas flow rate on platinum crucibles, with a heating rate of 10 °C/min and a scan range from 30 up to 700 °C. X-ray diffraction is used to identify the phases present in the samples. Data are collected from a Rigaku MiniFlex 600 X-ray diffractometer using a Cu-K_α source ($\lambda = 1.5405$ Å) operated with a voltage of 40 kV and a current of 15 mA. The XRD profiles are collected at $10° < 2\,\theta < 100°$, with a step of 0.1° The phases are identified by matching ICSD, COD (2014), and ICOD (1998) databases with High Score Plus software (v3.0). The morphology and elemental composition are studied by a scanning electron microscope (SEM) Thermo Scientific Scios 2 coupled to energy-dispersive spectroscopy (EDS). The metal content in the precursors and in the Pt/C ECs was determined by ICP-OES after acid digestion of the samples following EPA 3051–3052, using an iCAP PRO XP instrument from Thermo Scientific.

2.2. Synthesis of Pt/c ECs

2.2.1. Materials

Sodium hexachloroplatinate (IV) hexahydrate, which is obtained from Thermos Scientific (99.9 %) is used as a benchmark for micro-RAMAN studies and EC synthesis. For the microemulsion formulations, the oil phase is cyclohexane (99 %), the surfactant is hexadecyltrimethylammonium bromide – CTAB (98 %), 2-Butanol is used as the co-surfactant, and Sodium tetrahydridoborate is adopted as the reducing agent; all the chemicals are procured from Sigma-Aldrich, Germany. Ultrapure water is used throughout the experiments as the hydrophilic phase. The water-soluble platinum precursor labeled *"C1"*and procured form Altea Group is adopted for the formulation of microemulsions. The reactants used for the polyol synthesis are: (i) ethylene glycol – EG (Reag. USP, pH. Eur., 99.5 % v/v for analysis), which is procured from PanReac AppliChem; (ii) Polyvinylpyrrolidone – PVP (M_w: 40.000), which is purchased from MP Biomedicals; and (iii) the water-insoluble platinum precursors labeled *"C2"*and *"C3"* provided by Altea Group. Vulcan™ XC-72R is used as the carbon support for both synthetic methods and is obtained from Fuel Cell Store. The following

chemicals are used to wash the final Pt/C ECs: (i) ACS acetone; and (ii) ethanol absolute for analysis. Both chemicals are obtained from Merck. The Pt/C benchmark EC is HiSPEC™ 3000; it is procured from Alfa Aesar and has a nominal 20 wt % loading of Pt on Vulcan XC-72R. The ink preparation for RRDE studies also includes Nafion™ D520CS Alcohol based 1000 EW at 5 % weight (Ion Power D520) and isopropyl alcohol (IPA) for analysis (ACS ISO reagent, purchased from Merck). All the chemicals and materials used in this work are used as received.

2.2.2. Equivalent microemulsions synthesis

Two equivalent microemulsions are prepared to synthesize Pt/C ECs. The first contains cyclohexane (Oil Phase), 2-butanol (Cosurfactant), CTAB (Surfactant), and the C1 precursor dissolved in the aqueous phase. The second contains cyclohexane (oil phase), 2-butanol (Cosurfactant), CTAB (Surfactant), and $NaBH_4$ (Reducing Agent) dissolved in the aqueous phase. The CTAB with cyclohexane and 2-butanol (3:7 wt ratio) is mixed into a glass container for both systems. Then, they are placed in a warm bath at 55 °C, and the aqueous phase with the precursor and the RA is added at this temperature. The RA concentration is 15 mg/mL, while different concentrations of the precursors are evaluated to enhance the stability of microemulsion. A microwave pretreatment of the C1 platinum precursor is made in ammonium hydroxide at a pH of 11. Finally, both microemulsions are mixed at 55 °C, and after platinum reduction, Vulcan XC-72R is added to the solution and stirred for one hour at 900 rpm. The temperature dropped to 20 °C and the stirring continued for another 12 h. Finally, to separate the Pt/C EC, the solution is centrifuged at 6000 rpm in a Hettich EBA 20 centrifuge and washed four times with ethanol and three times with water.

2.2.3. Ternary diagram

A ternary diagram for the C1 precursor is devised to determine the stability area of the microemulsions. Thus, a mixture of CTAB and 2-butanol in a 3:7 wt ratio is added to the oil phase. Then, mixtures of Surfactant-Cosurfactant-Surfactant with weight ratios from 1:9 to 9:1 are blended in a glass test tube. A precursor solution is slowly added to the previous mix while stirring on a mechanical stirrer at 1200 rpm at different temperatures of 45 °C, 50 °C, and 55 °C. Finally, the aqueous phase is incorporated dropwise into the oil phase solution until a transparent and homogeneous dispersion is formed [27].

2.2.4. Polyol syntheses

The synthesis of Pt/C ECs is also carried out by means of a microwave-assisted polyol route using an Anton Paar microwave reactor Monowave 200 with an IR temperature sensor. Table 1 summarizes the reaction parameters of the present study. To synthesize the Pt/C ECs, 25 mg of the C2 or C3 precursors are dissolved in 6 mL of water. In addition, between 0 and 25 mg of PVP, acting as a capping agent, are dissolved into 6 mL of EG according to the statistical Design of Experiments (DoE). Both solutions are stirred (1000 rpm) for 10 min and mixed. 44 mg of Vulcan XC-72R are then added and the resulting suspension is ultrasonicated for 10 min. The final suspension is transferred to the microwave reactor, where the synthesis variables from Table S13 and Table S15 are programmed at a constant magnetic stirring of 1200 rpm. Subsequently, the suspension is stirred at 600 rpm for 24 h. The Pt/C EC is separated from the dispersion by washing for 30 min at 6000 rpm in a Hettich EBA 20 centrifuge three times with acetone and four times with water. Finally, the Pt/C EC is obtained by drying at 90 °C in a vacuum furnace for 12 h.

2.2.5. Statistical designs

A Box-Behnken design (BBD) is carried out to identify the optimal synthesis parameters to obtain high-performing Pt/C ECs for the ORR. Two factors are considered in the case of microemulsions (which include the precursor C1): (i) mass percentage of the aqueous phase; and (ii) precursor concentration at a temperature of 55 °C. On the other hand, three factors are considered in the case of polyols (which include either the C2 or the C3 precursor): (i) synthesis temperature; (ii) dwell time; and (iii) molar ratio between PVP and the $(NH_4)_2PtCl_6$ included in the precursor. The response variable evaluated for the three precursors is mass activity (MA). The latter is determined by the CV-TF-RRDE method [28] at a potential of 0.85 V. Table 1 summarizes the factors and levels for these three Design of Experiments (DoE).

2.3. Characterization of the Pt/c ECs

2.3.1. Physicochemical characterization

The vibrational features of the Pt/C ECs are evaluated using the micro-Raman spectrometer described in Section 2.1. The morphology and elemental composition are studied by a scanning electron microscope (SEM) Thermo Scientific Scios 2 coupled to energy-dispersive spectroscopy (EDS). High-resolution transmission electron microscopy (HR-TEM) studies are executed with a Jeol 3010 mounting a Gatan slow-scan 794 CCD camera. X-ray diffraction data are collected in an Antoon Paar XRD Dynamic 500 instrumentation using a Cu LFFK$_\alpha$ source operated with a voltage of 40 kV and a current of 15 mA. The diffractograms are fitted with the MAUD software [29]. TGA is performed in a TA instrument Q500 thermogravimetric analyzer, from 25 °C to 700 °C under an air atmosphere and at a scan rate of 20 °C·min^{-1}. The near-ambient pressure X-ray photoelectron spectroscopy (NAP-XPS) spectra are collected using an EnviroESCA instrumentation from Specs mounting an Al K$_\alpha$ excitation source ($h\nu$ = 1486.6 eV). The measurements are carried out at a pressure of *ca.* 10^{-6} mbar. The survey scans are obtained at a pass energy of 100 eV; each step has a width of 1.0 eV and the integration time is 0.1 s. High-resolution spectra are determined at a pass energy of 40 eV; each step has a width of 0.1 eV and an integration time of 0.5 s. The binding energy (BE) values are affected by an uncertainty of ±0.2 eV. The NAP-XPS profiles are fitted using the *"Keystone"* software provided by Specs. A Shirley-type background function is used [30]. Specs provide the sensitivity factors for integrated peak areas used for quantification purposes. The parameters are chosen to maximize the signal-to-noise ratio while ensuring that the samples do not undergo degradation triggered by X-ray exposure during the measurements [31].

2.3.2. Electrochemical characterization

Electrochemical measurements for the Box-Behnken Design are collected using the CV-TF-RRDE method [28]. First, the GC disk of the

Table 1
Summary of the synthetic parameters explored in the DoE.

Precursor	Level	Synthetic parameter				
		Aqueous phase / %	Precursor concentration / mg/mL	Temperature / °C	Dwell time / s	PVP/$(NH_4)_2PtCl_6$ / mol/mol
C1	−1	2.65	30	N/A		
	0	3.2	40			
	1	3.75	50			
C2 and C3	−1	N/A		120	150	0
	0			160	375	2
	1			200	600	4

rotating ring-disk electrode (RRDE) was coated with: (i) a Pt loading of 20 $\mu g_{Pt} \cdot cm^{-2}$ for C1 ECs (isopropanol, ECs, and ionomer mixture) and 15 $\mu g_{Pt} \cdot cm^{-2}$ for C2 and C3 ECs (7 to 3 ratio H_2O: Isopropanol, ECs, and ionomer mixture); and (ii) a 0.2 dry weight ratio between the Nafion™ D520CS ionomer and the Vulcan XC-72R used as the support in the ECs. The resulting suspension is homogenized using an ultrasonic probe for 2 min, followed by sonication in an ultrasonic bath for 3 h. Afterwards, the final dispersion is stirred for 24 h. Finally, a 6 μL drop of ink is deposited onto the GC electrode to form a uniform film. A standard three-electrode setup is used for all measurements, with the RRDE serving as the working electrode mounted on an RRDE-3A (BAS Inc.) system. The experimental collection efficiency of the Pt ring is measured as 0.43. The experiments are performed with two Ametek VersaSTAT 3F potentiostat/galvanostats. Initially, the electrode is cycled between 0.05 and 1.05 V *vs.* the reversible hydrogen electrode (RHE) in 0.5 M H2SO4 at 25 °C under pure O_2, with a sweep rate of 20 $mV \cdot s^{-1}$ at 1600 rpm of RRDE tip rotation. Cycling is continued until the voltammograms become stable. The acid solution is then discarded and replaced with a new 0.5 M H_2SO_4 solution to obtain the final voltammograms. The latter are collected in the same experimental conditions described above; the production of H_2O_2 is tracked by the ring electrode, which is polarized at 1.2 V *vs.* RHE. The faradic ORR currents are determined by subtracting the voltammograms recorded under O2 from those recorded under pure N_2 using the same electrode. iR correction is carried out by high-frequency EIS. The precise RHE potential is measured before each CV-TF-RRDE test. The counter electrode is a Pt wire. The disk currents are normalized on the geometric area of the GC. The reference electrode used is Ag/AgCl (NaCl sat.). The optimized Pt/C ECs obtained from C1, C2, and C3 were evaluated using the CV-TF-RRDE at a loading of 15 $\mu gPt \cdot cm^{-2}$ in a 7:3 H_2O:IPA solution with the appropriate amounts of the EC and ionomer. The RRDE tip is mounted on WaveVortex 10 Electrode Rotator (Pine Research Instrumentations). The collection efficiency of the Pt ring is equal to 0.39. The experiments are performed with a Bio-Logic VSP multichannel potentiostat/galvanostat in an acid solution of 0.1 M $HClO_4$, under pure O_2, at a temperature of 25 °C and at a sweep rate of 20 $mV \cdot s^{-1}$ with a $Hg/HgSO_4/K_2SO_{4(sat.)}$ reference electrode. CO_{ad} stripping measurements are performed by polarizing the electrode at 0.1 V *vs.* RHE for 10 min in a CO-saturated solution at $T = 25$ °C. Afterwards, the cell is purged with N_2 for 20 min while the working electrode polarization is maintained at 0.1 V *vs.* RHE. The CO molecules irreversibly adsorbed on the EC active sites are stripped by linearly increasing the working electrode's potential from 0.1 to 1.15 V *vs.* RHE at 50 $mV \cdot s^{-1}$. Then, the electrode is further cycled between 0.05 and 1.15 V *vs.* RHE at 20 $mV \cdot s^{-1}$ under pure N_2; the obtained profiles were subtracted from the CO_{ad} stripping trace to get the net stripping currents through which the electrochemically active surface area (ECSA) is evaluated. Accelerated ageing is carried out by cycling the RRDE tip in accordance with a triangular wave potential profile between 0.6 and 1.0 V at a sweep rate of 50 $mV \cdot s^{-1}$ under an inert atmosphere at $T = 25$ °C. The ORR performance and the ECSA are then determined as discussed above. ORR performance and ECSA are measured at the beginning of the measurements and after a total of 10, 100, 1000, 3000 and 10,000 accelerated ageing cycles [32].

3. Results and discussion

3.1. Characterization of C1, C2 and C3 precursors

The composition of the C1, C2 and C3 precursors provided by Altea Group is determined by Raman spectroscopy, infrared spectroscopy, and X-ray diffraction studies. Raman spectroscopy enables the identification of complexes present in the precursors (see Fig. 1(a)). The correlative assignment of the peaks, based on previous studies of platinum complexes [33], and the use of commercial sodium hexachloroplatinate(IV) hexahydrate spectra as a benchmark, clearly indicate that $PtCl_6^{2-}$ is the dominant complex in all the precursors. Indeed, all the spectra reveal the

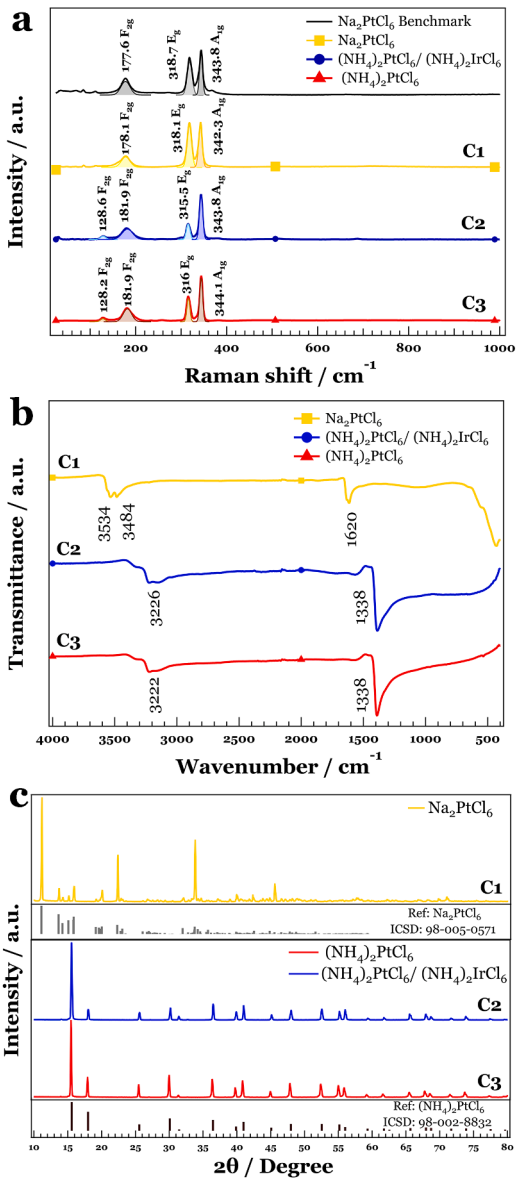

Fig. 1. Characterization of C1, C2 and C3 precursors. (a) micro-RAMAN profiles; (b) ATR FT-IR spectra; and (c) XRD patterns.

following modes, typical of the hexachloride complexes of PGMs: (i) ν_1 (A_{1g}, ≈ 344 cm^{-1}); (ii) ν_2 (E_g, ≈ 320 cm^{-1}); and (iii) ν_5 (F_{2g}, ≈ 180 cm^{-1}) [33,34]. Moreover, the presence of the bands at 181.9 cm^{-1} might indicate the presence of $RhCl_6^{3-}$ and the 128.2 cm^{-1} band might be ascribed to a skeletal vibration of $[Rh(NH_3)Cl_5]^{2-}$ complexes in both C2 and C3 impurities from the precursor preparation process [33–35].

Fig. 1(b) displays the infrared spectra of the precursors. C1 shows three bands at 3534, 3484, and 1620 cm^{-1}, corresponding, respectively, to the O—H symmetric stretching, the O—H antisymmetric stretching, and the O—H-O symmetric bending modes, indicative of the presence of hydration water [36]. Both C2 and C3 exhibit two bands. The former is located at 3222 cm^{-1} and corresponds to the ν_3 vibrational mode of the ammonium ion; the latter is observed at 1338 cm-1 and corresponds to the ν_4 vibrational mode of the same ion [37]. The EDS mapping of the C1, C2, and C3 precursors (see Figure S1-S3 and Table S2-S4 in Supporting Information) revealed the presence of impurities of other PGMs (*i.e.,* Rh and Ir), in agreement with micro-Raman spectroscopy results.

Fig. 1(c) shows the XRD profiles obtained for the C1, C2 and C3 precursors. The XRD profile of the C1 precursor matches that of the Na2PtCl6·6H2O phase; this is consistent with results from Raman

spectroscopy, FT-IR, and EDS mapping. On the other hand, the XRD profiles of the C2 and C3 precursors match the $(NH_4)_2PtCl_6$ phase; this is consistent with: (i) the results obtained by EDS mapping; (ii) the Raman mode of $PtCl_6^{-2}$; and (iii) the FT-IR modes of ammonium. It is also highlighted that the XRD profiles of chemicals comprising XCl_6^{2-} and XCl_6^{3-} complexes, where X = Pt, Pd, Rh and Ir are quite like one another [38–40]. Hence, it is tough to identify the presence of small impurities of species such as of $RhCl_6^{3-}$, and $IrCl_6^{3-}$ in the XRD profile of chemicals comprising $PtCl_6^{2-}$ anions (*e.g.*, $Na_2PtCl_6{\cdot}6H_2O$ – C1; and $(NH_4)_2PtCl_6$ – C2 and C3).

The complete thermogravimetric analysis (TGA) and ICP-OES analysis of the C1, C2 and C3 precursors is reported in Supplementary Information (see Section S2). To achieve a semiquantitative estimate of the purity of $Na_2PtCl_6{\cdot}6H_2O$ in C1, a mass balance is solved with the ICP-OES metal composition, which indicates the presence of 99.2 wt % of $Na_2PtCl_6{\cdot}6H_2O$. Correspondingly, $Na_2IrCl_6{\cdot}6H_2O$ and $Na_3RhCl_6{\cdot}12H_2O$ account for a total of 0.042 wt % (Table S6). Furthermore, C2 and C3 presented the thermal decomposition of $(NH_4)_2PtCl_6$ at 380 °C with traces of $(NH_4)_3RhCl_6$ and $(NH_4)_2IrCl_6$ (see Figure S4) [41]. For C3, the ICP-OES analysis shows a content of 75.43 wt % for $(NH_4)_2PtCl_6$ and of 1.9 wt % for $(NH_4)_2IrCl_6$ while $(NH_4)_3RhCl_6$ accounts for 0.08 wt % (Table S7). Finally, C3 includes 84.7 wt % of $(NH_4)_2PtCl_6$ and <0.09 wt % of $(NH_4)_2IrCl_6$ and $(NH_4)_3RhCl_6$. Despite these results, ICP-OES likely underestimates the content of Rh and Ir. However, the latter are likely included in the samples as chlorometalate complexes as revealed by micro-RAMAN (see Fig. 1(a)).

3.2. Results of the design of experiments (DoE)

3.2.1. Microemulsions including the C1 precursor

The microemulsion method is implemented to obtain Pt/C ECs starting from the C1 precursor, which is soluble in water. Due to the impurities present in the C1 precursor, the microemulsion method requires that *"stability zones"* are identified modulating: (i) the concentration of the C1 precursor; and (ii) the temperature. Fig. 2 illustrates the ternary stability diagrams for two C1 precursor concentrations and three temperatures.

It is found that at a lower concentration of the C1 precursor the stability zone is enlarged; however, higher amounts of surfactants, organic phase, and co-surfactant are necessary. Higher concentrations of the C1 precursor lead to narrower stability zones (see Fig. 2(b)). As the temperature rises, the stability zones are enlarged irrespectively of the concentration of the C1 precursor. It is also highlighted that the presence of sodium ions in microemulsion raises the ionic strength. Correspondingly, the equilibrium constants and the density of the aqueous phase are raised, while the reverse micromicelle volume changes. Despite all these issues, the systematic effort to identify experimentally the stability zones of microemulsions including a precursor obtained from mining residues and thus of non-analytical grade such as C1 is successful and allows for the preparation of Pt/C ECs.

Table S9 presents the ANOVA results for the mass activity (MA) of Pt/C electrocatalysts (ECs) synthesized via the microemulsion method with the C1 precursor, as shown in Fig. 3(a) and Fig. 3(b). The MA is significantly influenced by the aqueous phase percentage and C1 precursor concentration ($p \leq 0.05$), contributing to the narrow regions observed in the ternary diagrams. The statistical model demonstrates a strong agreement with experimental data (R^2 = 94.3 %, adjusted R^2 = 87.2 %), with deviations attributed to variations in the ECs film on the RRDE tip. Fig. 2 further reveals that simultaneous increases in both variables listed in Table 1 destabilize the microemulsion, thereby limiting the achievable precursor concentration. Moreover, dynamic light scattering (DLS) measurements (Figure S5) confirm that reverse micelle volume increases with higher C1 precursor concentration. However, excessive water content may promote crystal growth and micelle coalescence, leading to larger particles and a reduced electrochemically active surface area (ECSA), thereby lowering MA in the ORR [42,43] The Design of Experiments (DoE) identifies optimal synthesis conditions for high-performing Pt/C ECs as 55 °C temperature, 50 mg/mL $Na_2PtCl_6{\cdot}6H_2O$ concentration, and an aqueous phase mass percentage of 3.75 %.

3.2.2. Polyols for the C2 precursor

Pt/C ECs for the ORR were synthesized via the polyol method using the water-insoluble C2 precursor. The analysis of variance (ANOVA) for MA presented in Table S11 and supported by Figs. 3(c) and 3(d), identified the concentration of polyvinylpyrrolidone (PVP) and its interaction with temperature as the most significant factors affecting ORR performance. Both variables exhibited statistically substantial adverse effects on MA ($p \leq 0.05$, 95 % confidence level), with a model fit of R^2 = 90 %. Furthermore, the Pareto chart in Fig. 3(c) indicates that excess PVP reduces ORR activity. Although the C2 precursor yielded the highest-performing ECs, its synthesis was complicated by the presence of Rh and Ir complexes, limiting optimization flexibility compared to C1 and C3. Thermogravimetric analysis (Figures S12 and S14) revealed a mass loss between 160 °$C < T <$ 175 °C, attributed to residual PVP and other organic species such as ethylene glycol, despite post-synthesis washing (Section 2.2.4) [44]. These residues likely obstruct the active sites of Pt nanoparticles, thereby diminishing ORR efficiency [45]. Finally, the Design of Experiments (DoE) determined the optimal synthesis conditions for high-performance Pt/C ECs using the C2 precursor: temperature of 200 °C, dwell time of 375 s, and absence of PVP in the polyol. These findings are consistent with previous work by Karadeniz and Ayas [46] who demonstrated that elevated temperatures during microwave-assisted synthesis promote the formation and coalescence of multiple Pt nuclei into complex three-dimensional structures, thereby enhancing ORR activity.

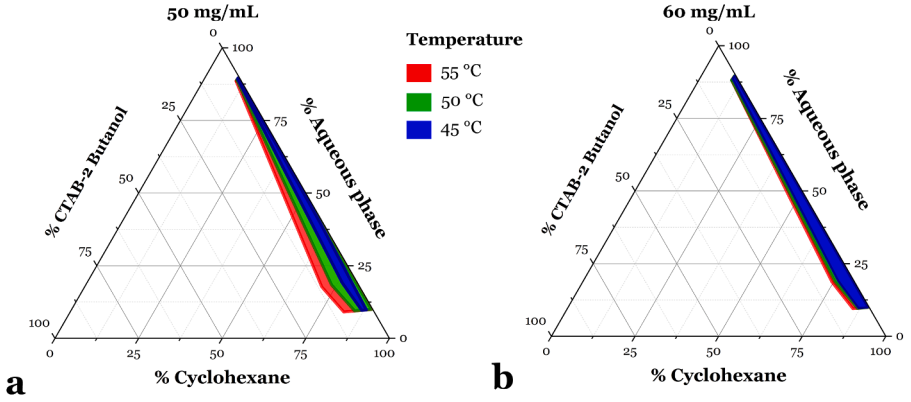

Fig. 2. Ternary diagrams displaying the concentration and temperature effects on the stability of the microemulsions including the C1 precursor. The concentration of the C1 precursor in the microemulsion is equal to: (a) 50 mg/mL and (b) 60 mg/mL.

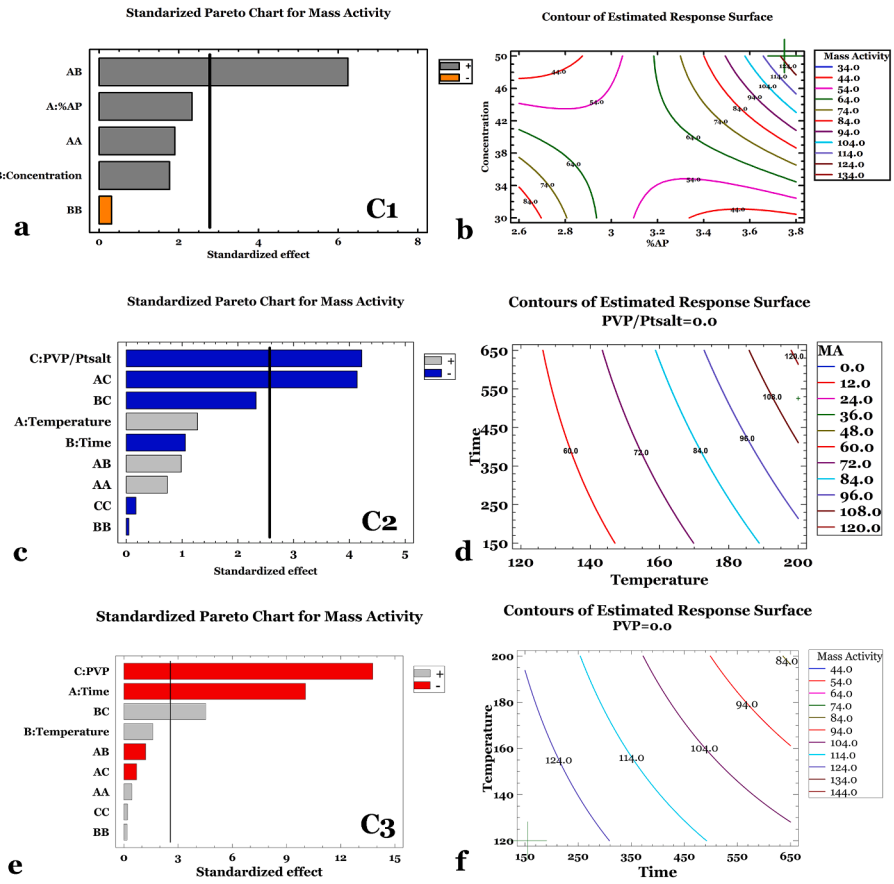

Fig. 3. DoE results for the Pt/C ECs including the C1, C2 and C3 precursors. C1: (a) Pareto chart, (b) contours response; C2: (c) Pareto chart, (d) contours response; and C3: (e) Pareto chart, (f) contours response.

3.2.3. *Polyols for the C3 precursor*

Table S13 presents the ANOVA analysis for the mass activity (MA) of Pt/C ECs synthesized via the polyol method using the C3 precursor, with Fig. 3(e) and Fig. 3(f) illustrating the performance trends. The most significant factors influencing oxygen reduction reaction (ORR) activity are the amount of PVP capping agent and the dwell time, both of which show statistical significance ($p \leq 0.05$, 95 % confidence). The model's R^2 is 98.4 %, adjusted to 95.6 % due to system variability, particularly in catalysts with higher rhodium content, which stabilize platinum distribution and reduce optimization variability (Table 15). The Design of Experiments (DoE) identifies optimal synthesis conditions as: 160 °C temperature, 150 s dwell time, and the absence of PVP. Despite PVP's known role in preventing nanoparticle coalescence, localized heating during microwave-assisted reduction enhances *in situ* structure and MA. Table 2 summarizes the best-performing synthetic parameters for Pt/C ECs derived from C1, C2, and C3 precursors.

3.3. *Morphology and composition of optimized Pt/c ECs for the ORR*

Fig. 4 displays SEM, HR-TEM, and STEM/EDS results of the optimized Pt/C ECs for the ORR obtained from the C1, C2, and C3 precursors. Fig. 4(a-g) refers to the optimized Pt/C EC for the ORR synthesized from the C1 precursor, labelled hereinafter as *"C1E3"*. SEM pictures show small bright spots associated with the Pt nanoparticle dispersion on the carbon support, indicating particle coalescence. Fig. 4 (b) shows that the morphology of the Pt nanoparticles, as revealed by HR-TEM, is spherical/ellipsoidal, as typical for ECs obtained with the microemulsion method [47]. The presence of Na_3RhCl_6 impurities at the micelles' interface during the synthesis likely gives rise to the ellipsoidal Pt nanoparticles. Fig. 4(c) reveals a lognormally distributed average particle size of 5.7 ± 1.7 nm, which is due to a slight aggregation of the Pt nanoparticles. The STEM/EDS distribution of the elements displayed in Fig. 4(d-g), and in particular the Pt map (see Fig. 4(f)) indicates Pt agglomeration in some regions of the carbon support observed in Fig. 4 (c).

Fig. 4(h-n) and Fig. 4(o-u) refer to the optimized Pt/C ECs for the ORR synthesized from the C2 and C3 precursors, labelled hereinafter as *"C2E9"* and *"C3E8"*, respectively. Fig. 4(i) and Fig. 4(p) confirm the presence of spherical Pt nanoparticles in both C2E9 and C3E8, whose average particle size is equal to 4.4 ± 1.0 nm (Fig. 4(j)) and 3.8 ± 1 nm (Fig. 4(q)), respectively. However, Pt NPs of C2E9 are very distinct, while the Pt NPs of C3E8 are somewhat attached. The STEM/EDS

Table 2
Optimized synthetic parameters yielding the best-performing Pt/C ECs for the ORR.

Precursor	Synthetic parameter				
	Aqueous phase / %	Precursor concentration / mg/mL	Temperature / °C	Dwell time / s	$PVP/(NH_4)_2PtCl_6$ / mol/mol
C1	3.75	50	N/A		
C2	N/A		200	375	0
C3	N/A		160	150	0

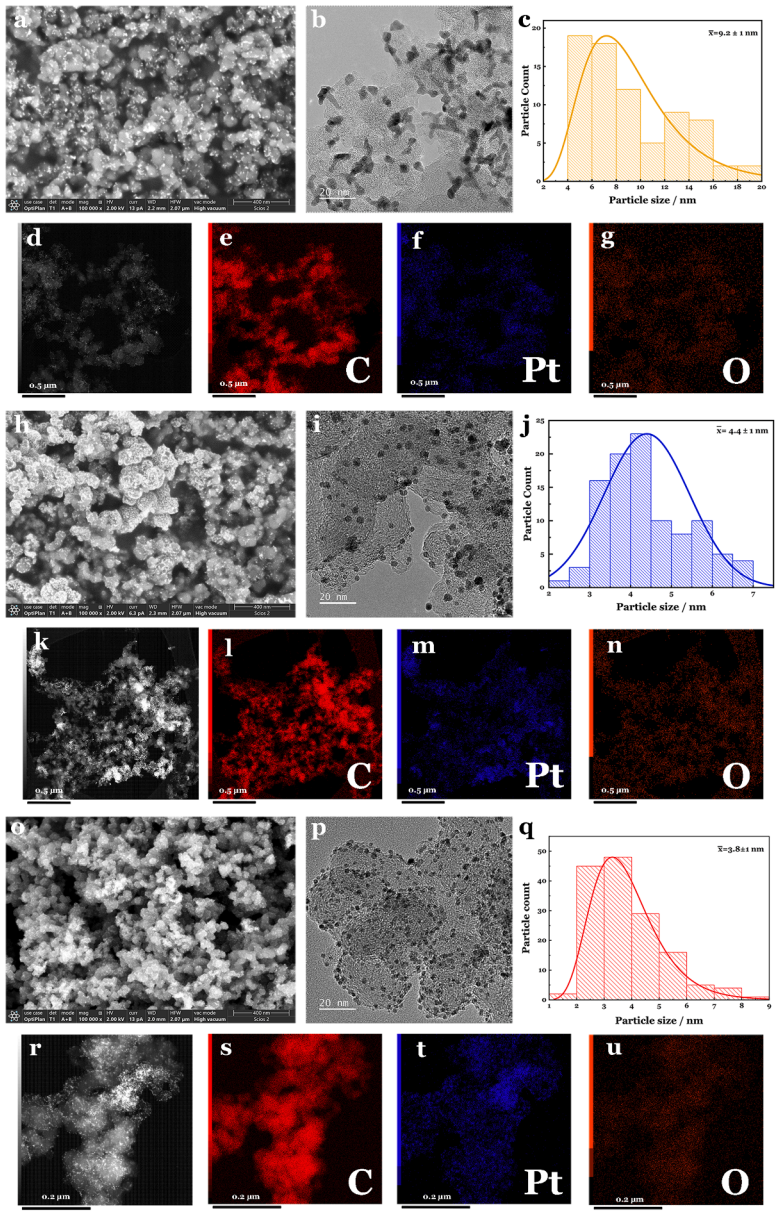

Fig. 4. Morphology and composition of optimized Pt/C ECs for the ORR. C1E3: (a) SEM; (b) HR-TEM; (c) particle size distribution; and (d-g) STEM/EDS composition. C2E9: (h) SEM; (i) HR-TEM; (j) particle size distribution; and (k-n) STEM/EDS composition. C3E8: (o) SEM; (p) HR-TEM; (q) particle size distribution; and (r-u) STEM/EDS composition.

distribution of the elements displayed in Fig. 4(k-n) and Fig. 4(r-u), respectively, for C2E9 and C3E8, indicates that, at a scale larger than that probed by HR-TEM, Pt nanoparticles are well distributed on the carbon support.

Distinctive differences between C1E3 (microemulsion) and C2E9 and C3E8 (polyol) Pt/C ECs for the ORR are that the latter exhibit: (i) a more uniform distribution of the Pt nanoparticles on the carbon support; and (ii) a smaller average particle size. This outcome is interpreted as indicating that the ethylene glycol medium in the polyol facilitates a more homogeneous nucleation of the Pt nanoparticles. Indeed, the high boiling point of the glycol ethylene medinum enables elevated synthesis temperatures. This promotes the controlled nucleation and growth of Pt nanoparticles by stabilizing the Pt-Pt dimers and the Pt_nCl_x intermediates, which are crucial during the nucleation phase [48,49]. The microemulsion method enables controlled nucleation and growth of Pt nanoparticles within nanoscopic aqueous domains stabilized by surfactants in a nonpolar medium. Reduction of Pt^{4+} by $NaBH_4$ occurs inside micelle cores, initiating nucleation [50,51]. The confined micellar environment limits particle growth, resulting in uniformly sized Pt nanoparticles. Graphite in the oil phase interacts with micelles via hydrophobic and electrostatic forces, especially at defect or functionalized sites, promoting micelle localization and Pt deposition near the graphite surface [51]. Although graphite serves as a support and nucleation substrate, it undergoes minimal oxidation, leading to more pronounced nanoparticle growth and thus larger Pt particle sizes. Figures S6-S11 report additional information on the morphology of the optimized Pt/C ECs for the ORR obtained starting from the C1, C2, and C3 precursors.

ICP-OES (see Table S16) does not reveal a significant amount of Rh and Ir in C1E3, C2E9, and C3E8. The small amounts of chlororhodate or chloroiridate complexes found in the starting C1, C2, and C3 precursors do not undergo significant reduction during the synthetic process yielding the optimized Pt/C ECs for the ORR. This outcome is interpreted considering that chlororhodate and chloroiridate complexes are both highly stable and kinetically inert [35,52]. In the case of

microemulsions (such as that used in the synthesis of C1E3), the reduction of chlororhodate and chloroiridate complexes requires several concurring phenomena, including: (i) a dynamic interaction where two reverse micelles interchange the material inside them; and (ii) the presence of a potent reducing agent and also H_2 bubbling [53] or a different hydrocarbon phase, such as n-Hexane/Isooctane, to destabilize the complexes and expose the metal center [54]. In the case of polyols (such as those used in the synthesis of C2E9 and C3E8), the reduction of chlororhodate and chloroiridate complexes cannot be achieved only by means of the ethylene glycol medium; this is particularly the case for Rh, as shown in the literature [55]. Indeed, chlororhodate and chloroiridate complexes stabilize in ethylene glycol media due to the coordinating ability of polyols. The latter favors the solubility of metal ions through the formation of metal complexes, thus avoiding the reduction of the Rh/Ir metal center. As a result, the reduction of Rh would require other reducing agents (*e.g.*, ascorbic acid and citric acid), together with the introduction of KBr [55]. Similarly, the reduction of chloroiridate complexes requires more potent reducing agents than ethylene glycol such as trisodium citrate or polyethylene glycol [52].

As a conclusion, under the synthesis conditions used to obtain the optimized Pt/C ECs for the ORR based on the C1, C2 and C3 precursors, the chlororhodate and chloroiridate complexes found in the latter could not be reduced and neither Rh nor Ir are introduced into the C1E3, C2E9 and C3E8 ECs.

Fig. 5 displays high-magnification HR-TEM images of the optimized Pt/C ECs for the ORR, together with the corresponding Fast Fourier Transform images. C1E3, C2E9 and C3E8 all reveal the usual interplanar distances ascribed to Pt(111), Pt(200), Pt(220) and Pt(222). Thus, C1E3, C2E9 and C3E8 all include fcc Pt nanoparticles.

Fig. 6 illustrates the x-ray diffractograms of the Pt/C benchmark and of the optimized Pt/C ECs for the ORR. Table 3 summarizes the results of the analysis with the MAUD software [29] of the x-ray diffractograms displayed in Fig. 6.

The XRD results are in accordance with the outcome of the FFT analysis of the high-magnifiction HR-TEM images displayed in Fig. 5. The XRD profiles of the Pt/C benchmark EC and the Pt/C ECs for the ORR, based on the C1, C2, and C3 precursors, are very similar to one another and display the same peaks. The latter associated to two phases: (i) platinum nanocrystals with an fcc structure, revealing the usual (111), (200) and (220) reflections [56]; and (ii) nanometric graphite from the XC-72R carbon used as the support, which shows the (002) and (101) reflections [57]. It is concluded that both the optimized micro-emulsion and the optimized polyol synthetic approaches yield Pt/C ECs for the ORR characterized by a very similar long-range order compared to the Pt/C benchmark.

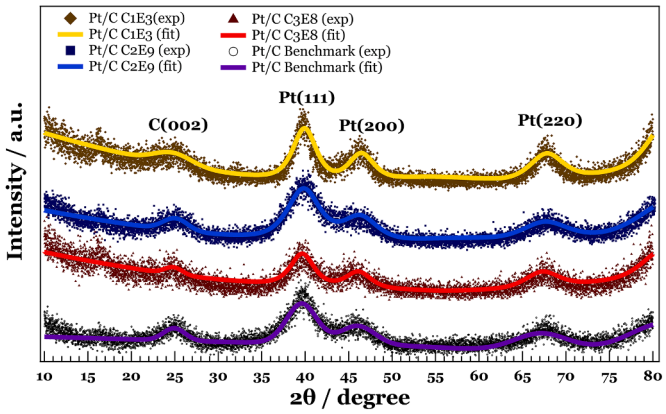

Fig. 6. XRD profiles of the Pt/C benchmark and of the optimized Pt/C ECs for the ORR obtained from the C1, C2 and C3 precursors.

The survey XPS spectra of both the proposed ECs and the Pt/C benchmark are displayed in Fig. 7(a). The profiles allowed for the determination of the surface chemical composition, which is reported in Table 4.

The majority component of all the ECs is C. All the ECs also include: (i) Pt, from the platinum nanoparticles bearing the active sites; (ii) O; and (iii) a very small amount of S, <0.5 at %, provided by the Vulcan XC-72R used as the support (this is consistent with the results reported in Table S16). The surface of C3E8 also includes 3.7 at % of N, likely

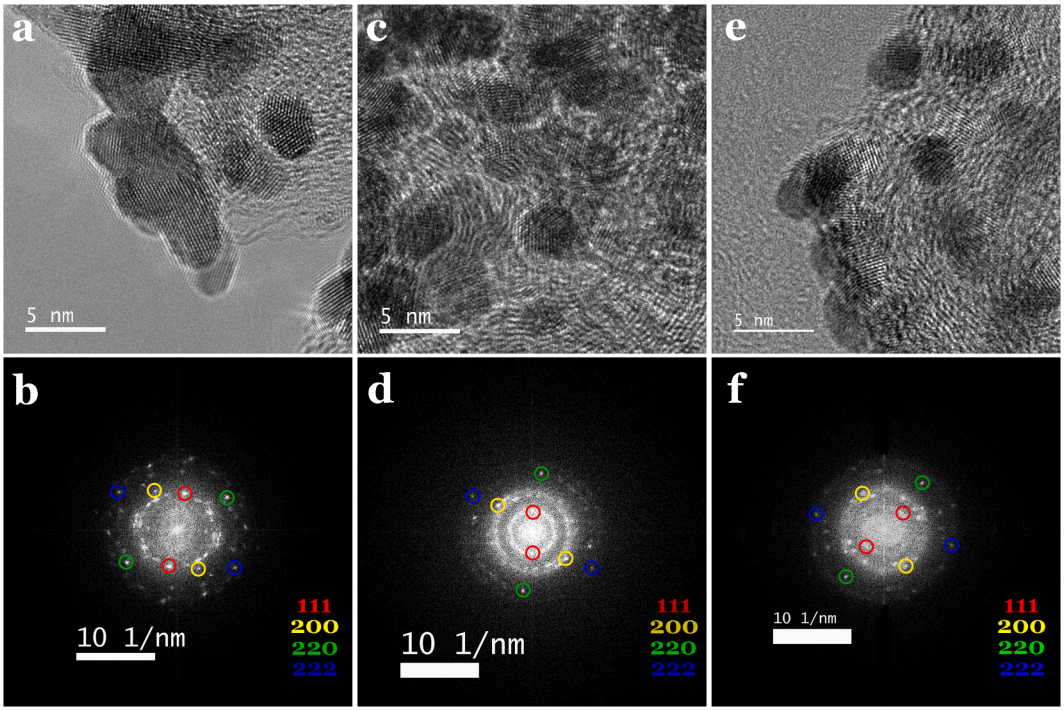

Fig. 5. Fast Fourier Transform (FFT) analysis of high-magnification HR-TEM images. (a) HR-TEM of C1E3; (b) FFT of C1E3; (c) HR-TEM of C2E9; (d) FFT of C2E9; (e) HR-TEM of C3E8; and (f) FFT of C3E8.

Table 3
Results of the analysis of the x-ray diffractograms displayed in Fig. 6.

	XRD			
Electrocatalyst	Composition / wt %	d-spacing	2θ	Peaks
Pt/C benchmark	C: 84	3.57 Å	24.91	C(002)
		1.70 Å	53.95	C(101)
	Pt: 16	2.27 Å	39.74	Pt(111)
		1.96 Å	42.22	Pt(200)
		1.39 Å	67.43	Pt(220)
Pt/C C1E3	C: 80	3.61 Å	24.61	C(002)
		1.70 Å	53.79	C(101)
	Pt: 20	2.26 Å	39.76	Pt(111)
		1.96 Å	46.24	Pt(200)
		1.39 Å	67.48	Pt(220)
Pt/C C2E9	C: 81	3.61 Å	24.64	C(002)
		2.19 Å	41.09	C(101)
	Pt: 19	2.26 Å	39.82	Pt(111)
		1.96 Å	46.31	Pt(200)
		1.39 Å	67.57	Pt(220)
Pt/C C3E8	C: 84	3.57 Å	24.91	C(002)
		1.70 Å	53.95	C(101)
	Pt: 16	2.27 Å	39.74	Pt(111)
		1.96 Å	42.22	Pt(200)
		1.39 Å	67.43	Pt(220)

deriving from the ammonium precursor used for this latter EC. It is pointed out that the content of O increases in the order: C1E3 < C3E8 ≈ Pt/*C* < C2E9.

The high-resolution XPS profiles of Pt 4f, C 1 s, and O 1 s undergoes decomposition to better elucidate the chemical state of the surface atoms of the ECs. Pt 4f exhibits a doublet (see Fig. 7(b)), whose peaks are centered at 71.4 eV (Pt $4f_{7/2}$ transition) and 74.7 eV (Pt $4f_{5/2}$ transition). Each peak comprises three components associated with Pt(0), Pt(II), and Pt(IV) species, and their relative abundance is shown in Fig. 7(c). In detail, the doublets ascribed to Pt(0), Pt(II) and Pt(IV) peak at: (i) 71.4 and 74.7 eV; (ii) 72.4 and 75.7 eV; and (iii) 73.7 and 77.0 eV [58,59]. In all the ECs, the prevalence of Pt(0) and Pt(II) is quite similar (approximately 40–50 at %); on the other hand, the prevalence of Pt(IV) is significantly lower (approximately 5–10 at %). Though the overall chemical state of Pt species is relatively similar in all the ECs, the prevalence of oxidized species (Pt(II) + Pt(IV)) rises slightly in the order: C2E9 < C1E3 < C3E8 < Pt/C. The peak ascribed to the C 1 s transition includes several components (see Fig. 7(d)), whose binding energy is increased as follows: sp^2 < sp^3 < *C*—*O* < epoxide < *C* = *O* < COOH < π-π* [60–62].

The relative abundance of such components is reported in Fig. 7(e); it is highlighted that the π-π* peak contributes to the abundance of the sp^2 species. Overall, it is found that the prevalence of oxidized carbon species increases in the order Pt/*C* ≈ C1E3 < C3E8 < C2E9. In particular, in C2E9 the prevalence of highly oxidized carbon species (*e.g.*, epoxide, *C* = *O* and COOH) is 3–5 times larger than that of the other ECs.

Finally, the peak of the O 1 s transition can be decomposed into four components (see Fig. 7(f)), whose binding energies are in the following order: *C* = *O* < *C*—*O* < *O*—*C* = *O* < Ads. H_2O [63–65]. The relative abundance of such components is displayed in Fig. 7(g). It is found that: (i) the prevalence of the *C* = *O* species decreases in the order: C1E3 > Pt/*C* > C3E8 > C2E9; and (ii) the relative abundance of the C—O species increases as follows: C2E9 < C1E3 < C3E8 < Pt/C. Finally, C2E9 is the only EC exhibiting a clear component ascribed to adsorbed H_2O in the O 1 s transition.

Based on these results and the discussion of particle size growth, Fig. 7 indicates that as graphite oxidizes during synthesis, the sp^2 atom percentage decreases relative to the Pt/C benchmark. The presence of Pt (0) species increases as C2E9 presents the lower sp^2 and the higher Pt(0) atom percentage (Fig. 7(c) and 7(e)). Furthermore, the graphite oxidation for this EC appears to be associated with epoxide and *C* = *O* formation, as evidenced by the C 1 s spectra and corroborated by O 1 s O—*C* = *O* in the graphite, which shows a higher atom percentage than the rest of the materials. Therefore, Pt(II) seems to be associated with the C—O sites as C 1 s and O 1 s indicated, the highest Pt(II) content is for the C3E8 material which presented the highest C—O atomic percentage and the lowest COOH sites. This suggests that during the reduction steps from Pt (II) these sites anchor and isolated the Pt(II) species, thus inhibiting Pt (0) formation. Finally, C1E3 showed higher sp^2 and sp^3 carbon, indicating less oxidized carbon support than in the polyol methods. However, this might also explain the higher particle size observed, where the anchor nanoparticles exhibit greater growth after nucleation. The lower atomic percentage of O—*C* = *O* might indicate that these sites could be possible anchors in the carbon structure that allow the Pt(II) to Pt(0) reduction in the polyols method; this could be the origin of the higher presence of Pt(II) for this EC.

3.4. Electrochemical performance

Fig. 8 and Table 5 summarize the electrochemical performance of the optimized Pt/C ECs for the ORR obtained with the C1, C2, and C3 precursors as compared with the Pt/C benchmark. Figure S15 and Table S10 report the outcome of the DoE for the ECs prepared with the C1 precursor. The limiting current density plateau ranges from −4.25 V to −4.81 V, with minor fluctuations between these values. Figure S16 and Table S12 summarize the DoE results for the ECs prepared with the C2 precursor. There are differences in the limiting current values of each EC due to slightly different mass-transport limitations at the ionomer/electrocatalyst interfaces, associated with morphological differences, such as nanoparticle distribution and agglomerates [66].

Besides, according to the DoE, a decrease in $E(j_{Pt}(5\ \%))$ is observed for the ECs where PVP is introduced as the capping agent in the polyol. This decrease is ascribed to the blocking of some Pt active sites by PVP, which is not entirely removed by the final washing (also see Section 3.2.2.) [45]. Figure S17 and Table S14 include the DoE results for the ECs prepared with the C3 precursor. Although these Pt/C ECs exhibit a higher mass activity in the DoE, their performance when compared with the best-performing Pt/C ECs is not as good as expected. This outcome might be associated with a low ECSA, triggered by some aggregation between the Pt nanoparticles bearing the active sites.

Furthermore, all optimized Pt/C ECs (C1, C2, C3) show lower ring currents than the Pt/C benchmark (Fig. 8(a)), resulting in smaller peroxide fractions and electron numbers closer to 4 (Fig. 8(b)). This outcome is confirmed by Koutecky–Levich experiments (Figures S18–S21, Table S18), which reveal a similar selectivity for the 4-electron ORR mechanism than Pt/C. The cyclic voltammograms of C1E3, C2E9 and C3E8 in an inert atmosphere (Fig. 8(c)) reveal the usual features of nanocomposite Pt/C ECs such as the benchmark. The ECSA determined by CO_{ad} stripping (Fig. 8(d), Table 5) follows the order: C1E3 ≈ C3E8 < Pt/*C* < C2E9, with all ECs showing CO_{ad} stripping peaks at ~0.85 V, suggesting similar active site chemistry and intrinsic ORR kinetics based on SA@0.9 V [68]. The SA@0.9 V of the ECs follows the trend: C2E9 < C1E3 ≈ C3E8 < Pt/C benchmark (Table 5). Despite slight differences, values are comparable to those reported for ORR ECs with pure Pt nanoparticles [68], consistent with (i) similar Pt chemical states (Fig. 7(b) and Fig. 7(c)) and (ii) absence of co-catalysts [68]. C2E9 shows the lowest SA@0.9 V due to abundant oxygen (Table 4) and highly oxidized carbon species (Fig. 7(d) and Fig. 7(e)), which act as electron traps, inhibiting O_2 reduction. For C1E3 and C3E8, the decreased SA@0.9 V (Table 5) is likely linked to a higher proportion of *C* = *O* and O–*C* = *O* groups relative to C–O (Figs. 7(f), 7(g)), suggesting these groups more effectively trap electrons, slowing ORR kinetics. The overall performance of Pt-based ORR ECs is assessed by $E(j_{Pt}(5\ \%))$ [69] and MA@0.9 V [68], which correlate with ECSA (number of active sites) and SA@0.9 V (intrinsic kinetics). Both metrics increase as: C1E3 ≈ C3E8 < Pt/*C* ≈ C2E9 (Table 5). The lower ECSA of C1E3 and C3E8 (~30 m^2/g_{Pt}) limits performance despite good SA@0.9 V (~450 mA/cm^2_{Pt}). Conversely, C2E9 compensates for slower kinetics with a very large ECSA (92 m^2/g_{Pt}) and more active sites than Pt/C.

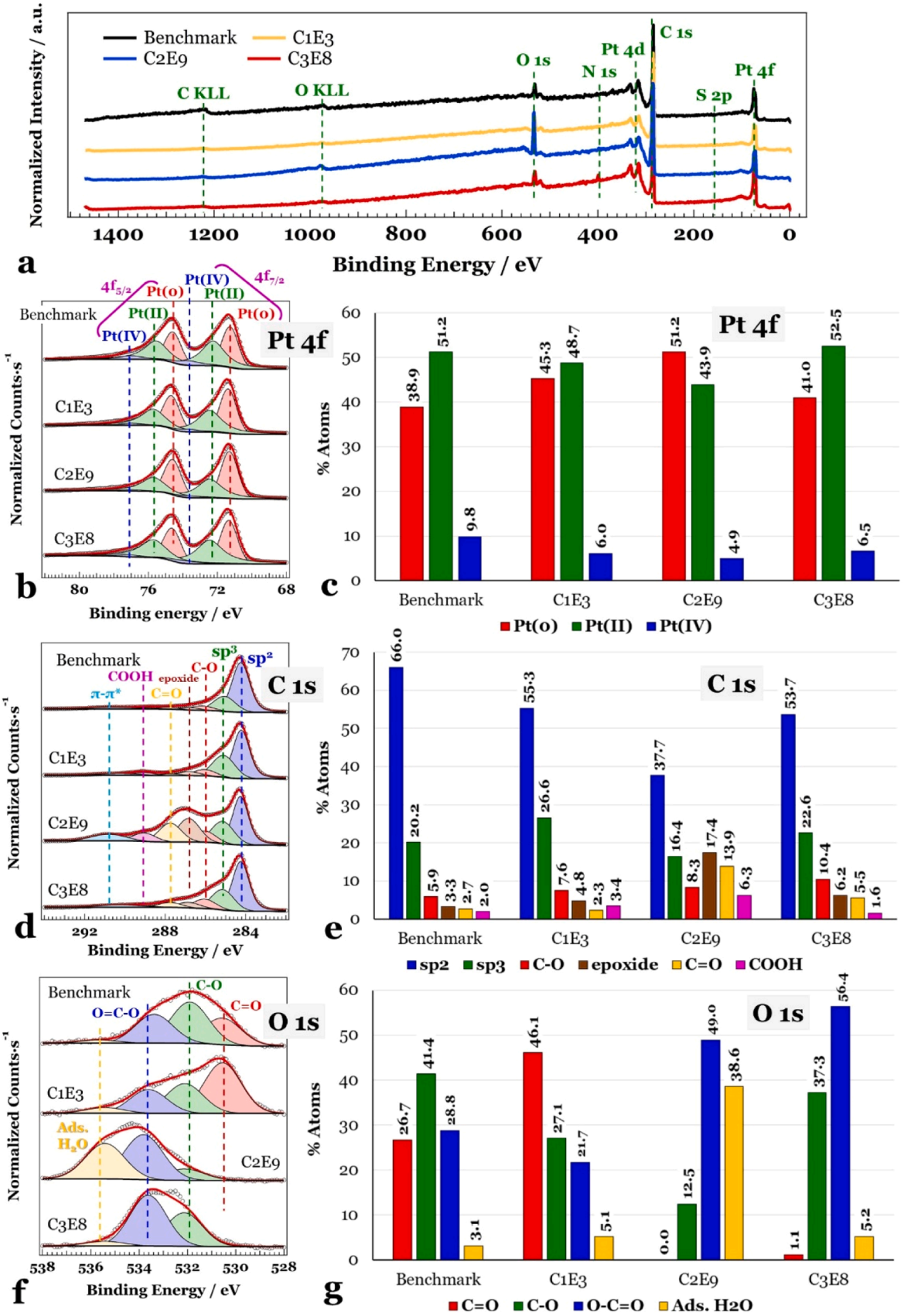

Fig. 7. (a) Survey XPS spectra of the ECs and of the Pt/C benchmark. Decomposition of the high-resolution profiles determined by NAP-XPS of the ECs and of the Pt/C benchmark: (b) Pt 4*f*; (d) C 1*s* ; (f) O 1*s* . % of atoms in the various chemical states: (c) Pt 4*f*; (e) C 1*s* ; (g) O 1*s* .

Table 4
Surface chemical composition of the ECs.

Electrocatalyst	At %					Surface Stoichiometry
	Pt	C	O	N	S	
Pt/C Benchmark	2.8	89.7	6.9	0.0	0.5	$PtC_{31.5}O_{2.4}S_{0.18}$
C1E3	1.9	92.0	5.9	0.0	0.2	$PtC_{49.4}O_{3.2}S_{0.11}$
C2E9	1.5	83.9	14.3	0.0	0.3	$PtC_{54.3}O_{9.3}S_{0.19}$
C3E8	3.4	86.0	6.6	3.7	0.4	$PtC_{25.4}O_{1.9}N_{1.1}S_{0.11}$

Fig. 8(f) shows CO_{ad} stripping evolution for ECSA (Table 5). After 10,000 accelerated ageing cycles, ECSA retention exceeds 89 % across all ECs, similarly to the benchmark (Fig. 8(g)). This indicates that cycling, despite triggering some changes in mass activity, does not lead to an excessive agglomeration of the Pt nanoparticles bearing the active sites. C2E9 and C3E8 recover MA after 3000 accelerated ageing cycles (Fig. 8(h)), while C1E3 shows 52 % MA decay, likely due to particle coalescence from its larger initial size. Intermediate MA decay (up to 36 %) in C2E9 and C3E8 is followed by recovery, possibly due to Pt(II) redistribution at O–*C* = *O* sites formed during polyol synthesis, as supported by XPS. ORR diffusion-limited current is lower than the benchmark (Figure S22), suggesting a slightly inhibited O_2 transport, especially for C1E3 post-cycling. Finally, $E(j_{Pt}(5\ \%))$ [69], which is a relevant figure of merit to gauge the kinetic behavior of the ECs, indicates that in all the electrocatalysts the ORR overpotential increases upon cycling. A final recovery at 10,000 cycles is observed in C2E9 and C3E8 due to active sites reaccommodation and recovery as discussed above.

The outcome of the experiments reported in this work suggests that to maximize the ORR performance of Pt/C ECs prepared starting from precursors obtained from mining residues it is preferred to: (i) start from a Pt complex that is insoluble in water (*e.g.*, the $(NH_4)_2PtCl_6$ found in

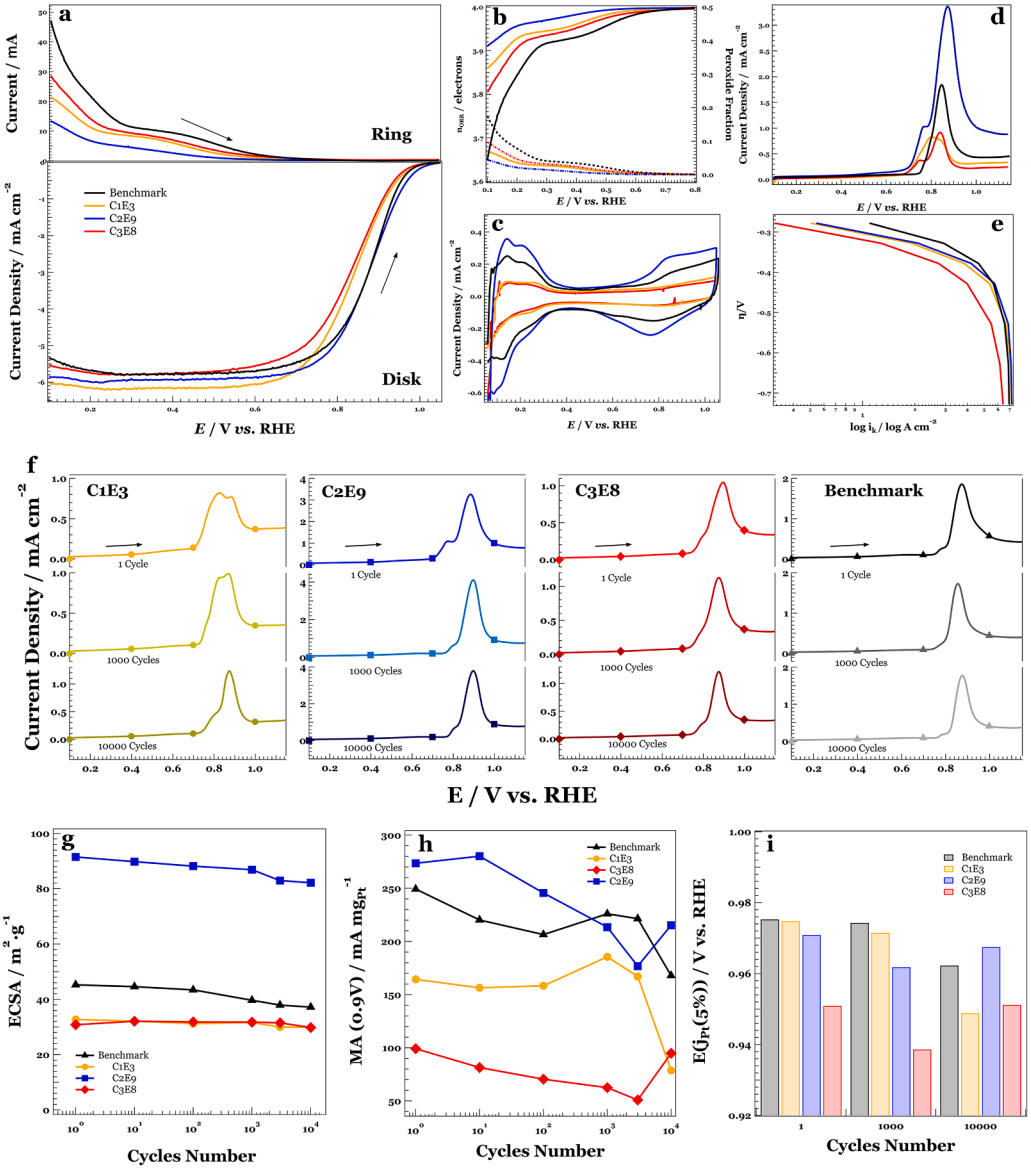

Fig. 8. (a) Performance of the optimized Pt/C ECs obtained from the C1, C2, and C3 precursors. The upper traces show the oxidation currents measured at the Pt ring of the RRDE. The lower traces are the ORR current densities measured on the glassy carbon disk of the tip. $P_{O2} = 1$ atm; the RRDE is rotated at 1600 rpm. (b) Average number of electrons exchanged in the ORR (left); fraction of H_2O_2 (peroxide) formed during the ORR (right). (c) Cyclic voltamograms under N_2. (d) CO_{ad} stripping current densities of the proposed ECs. (e) Tafel plot of the ECs. (f) CO_{ad} stripping for the aging ECs. (g) ECSA evolution with ageing. (h) Mass activity evolution with aging. (i) Variation in $E(j_{Pt}(5\ \%))$ after 10,000 cycles. All electrodes have a Pt loading of 15 μg·cm^{-2}. A 0.1 M $HClO_4$ solution fills the electrochemical cell at 25 °C; the sweep rate is 20 mV·s^{-1}. The electrode tip is not rotated during CO_{ad} stripping. $P_{N2} = 1$ atm. The other experimental conditions are described in the literature [67].

Table 5
Figures of merit describing the ORR performance of the optimized Pt/C ECs obtained from the C1, C2, and C3 precursor.

Electrocatalyst	#Cycles	MA@0.9 V (mA/mg_{Pt})	MA Decay (%)	E(j_{Pt}(5 %))	ECSA (m^2/g)	ECSA Retention (%)	SA@0.9 V (mA/cm^2)
C1E3	1	164.4	–	0.975	32.7	–	502.0
	1000	185.6	−12.9	0.972	31.6	96.6	587.5
	10,000	78.7	52.1	0.949	29.9	91.4	263.3
C2E9	1	273.5	–	0.971	91.5	–	323.2
	1000	213.5	21.9	0.962	86.9	95.0	278.4
	10,000	215.3	21.3	0.968	82.2	89.8	300.7
C3E8	1	99.1	–	0.951	30.8	–	321.8
	1000	62.5	36.9	0.939	31.8	103.2	196.7
	10,000	94.8	4.3	0.951	29.8	96.7	318.1
Benchmark	1	249.3	–	0.975	45.3	–	337.2
	1000	226.0	9.3	0.974	39.7	87.6	348.7
	10,000	167.9	32.7	0.962	37.2	82.1	276.2

C2); and (ii) oxidize the surface of the carbon support (in our case, Vulcan XC-72R) using the polyol method assisted by a vigorous microwave treatment ($T = 200\ ^\circ C$, dwell time = 375 s) and in the absence of a capping agent (see Table 2). These synthesis conditions likely leads to a high density of oxidized species on the carbon support surface. Such oxidized species then act as abundant nucleation sites for the growth of many small, well-dispersed Pt nanoparticles, yielding a large ECSA (corresponding to a large number of ORR active sites) at the expense of somewhat reduced intrinsic ORR kinetics for each active site. The final result is C2E9, a Pt/C EC for the ORR, whose overall performance compares favorably with that of the Pt/C benchmark and is also more selective towards the 4-electron mechanism.

4. Conclusions

This work demonstrates a sustainable approach to obtain high-performance Pt/C electrocatalysts for the ORR by valorizing mining residues as Pt precursors. Comprehensive characterization confirmed high Pt content with minor PGM impurities, enabling synthesis via microemulsion and microwave-assisted polyol methods. Using Box–Behnken optimization to tune key synthetic parameters, we established robust protocols to tailor particle size, dispersion, and surface chemistry. These findings highlight the feasibility of converting mining waste into advanced electrocatalysts, reducing environmental impact while maintaining competitive performance, an essential step toward circular economy strategies in energy-conversion technologies.

The optimized Pt/C electrocatalysts (C1E3, C2E9, C3E8) exhibit structural and chemical features comparable to the state-of-the-art Pt/C benchmark, including Vulcan XC-72R support, ~20 wt % Pt loading, and similar Pt surface states (XPS). Among them, C2E9 shows comparable performance, with E(j_{Pt}(5 %) = 0.971 V and MA@0.9 V = 273.5 mA/mg_{Pt}, barely surpassing the Pt/C benchmark (E(j_{Pt}(5 %) = 0.975 V, MA@0.9 V = 249.3 mA/mg_{Pt}), while C1E3 and C3E8 remain competitive. These results are interpreted acknowledging that, relative to the Pt/C benchmark, the carbon support in C2E9 is more oxidized, which favors the formation of smaller, well-dispersed Pt nanoparticles during synthesis. Consequently, with respect to the Pt/C benchmark, the ECSA of C2E9 is larger (91.5 m^2/g_{Pt} *vs.* 45.3 m^2/g_{Pt}).

Furthermore, durability analysis confirms that all optimized Pt/C electrocatalysts retain *ca.* 90 % of their ECSA after 10,000 accelerated ageing cycles, demonstrating an excellent stability. The main difference lies in mass activity decay: C1E3 shows the highest loss (52 %), while C2E9 and C3E8 outperform the Pt/C benchmark with a lower decay and partial recovery after 3000 accelerated ageing cycles. Notably, these materials maintain a competitive performance even under extended cycling, highlighting their durability and suitability for long-term operation in practical fuel cell applications.

In conclusion, this work demonstrates that by a suitable optimization of the synthetic parameters it is possible to use impure precursors obtained from mining residues to obtain viable Pt/C ECs for the ORR, whose performance compares favorably with that of a state-of-the-art commercial benchmark. In perspective, this could lead to diversification of Pt suppliers, thereby helping curb the costs of PEMFC electrodes and facilitating the large-scale rollout of this promising green energy technology.

CRediT authorship contribution statement

Diana Orozco-Gallo: Conceptualization, Formal analysis, Investigation, Methodology, Writing – original draft, Writing – review & editing. **Ricardo Ossa-Gallego:** Investigation, Methodology, Writing – original draft. **Catalina Orozco-Silva:** Investigation, Methodology, Writing – original draft. **Verónica Muñoz-Montes:** Investigation, Writing – original draft. **Soufiane Boudjelida:** Investigation, Methodology. **Gioele Pagot:** Formal analysis, Investigation, Methodology. **Enrico Negro:** Formal analysis, Methodology, Writing – original draft, Writing – review & editing. **Vito Di Noto:** Conceptualization, Formal analysis, Investigation, Methodology, Writing – review & editing. **Jorge A. Calderón:** Conceptualization, Funding acquisition, Methodology, Supervision, Writing – review & editing.

Declaration of competing interest

The authors declare the following financial interests/personal relationships which may be considered as potential competing interests:

Jorge Andres Calderon Gutierrez reports financial support was provided by Government of Colombia Ministry of Treasury and Public Credit. Diana Constanza Orozco Gallo reports financial support was provided by Government of Colombia Ministry of Treasury and Public Credit. Ricardo Ossa Gallego reports financial support was provided by Government of Colombia Ministry of Treasury and Public Credit. Catalina Orozco Silva reports financial support was provided by Government of Colombia Ministry of Treasury and Public Credit. Veronica Munoz Montes reports financial support was provided by Government of Colombia Ministry of Treasury and Public Credit. Jorge Andres Calderon Gutierrez reports equipment, reagents, or supplies was provided by Grupo Altea SAS - Colombia. Vito Di Noto reports financial support was provided by Government of Italy Ministry of University and Research. Vito Di Noto reports financial support was provided by Italian Recovery and Resilence Plan. Porfessor Vito Di Noto is a guest editor for this special issue. "Given his role as guest editor, he had no involvement in the peer review of this article and had no access to information regarding its peer review. Full responsibility for the editorial process for this article was delegated to another journal editor." If there are other authors, they declare that they have no known competing financial interests or personal relationships that could have appeared to influence the work reported in this paper.

Acknowledgments

The authors thank "Ministerio de Ciencia Tecnología e Innovacion - Minciencias" for the financial support provided by 25 2021–2022 and "Ministerio de Hacienda - Minhacienda" call for the strengthening of CTeI in public higher education institutions under the project: *"Desarrollo y apropiación de tecnologías convergentes para la generación del conocimiento y la infraestructura necesarios para almacenar energía solar en forma de hidrógeno verde, así como para el uso de este vector energético a nivel nacional"* BPIN 2022000100089. Furthermore, we would like to acknowledge the company Grupo Altea SAS for providing the precursors to develop this work. This work also received funding under: i) the National Recovery and Resilience Plan (NRRP), Mission 4 Component 2 Investment 1.4 – Call for tender No 3138 of December 16, 2021 of the Italian Ministry of University and Research, funded by the European Union – NextGenerationEU [Award Number: CNMS named MOST, Concession Decree No 1033 of June 17, 2022, adopted by the Italian Ministry of University and Research, CUP: C93C22002750006, Spoke 14 "*Hydrogen and New Fuels*"]; ii) the project "*PERMANENT*" financed in the framework of the Italian PNRR, M2C2, Investment Line 3.5; iii) Project *"DURALYS - DURAble, Scalable, and Recyclable Component sand Cell Designs for Next Generation Alkaline Exchange Membrane Water Electrolysis"* funded under the German- Italian Joint call for proposals on *"Green Hydrogen Research: A Collaboration to Empower Tomorrow's Energy"* within the framework of the collaboration between the German Federal Ministry of Education and Research (BMBF), the Italian Ministry of Foreign Affairs and International Cooperation (MAECI) and the Italian Ministry of University and Research (MUR) and iv) the PRIN2022 project *"Alkaline membrane–electrode assemblies for fuel cells (ALEF)"* (Prot. 2022PYXHYL) of the Italian Ministry of University and Research (MUR)."

Supplementary materials

Supplementary material associated with this article can be found, in the online version, at doi:10.1016/j.electacta.2025.147979.

Data availability

Data will be made available on request.

References

[1] P. Atanassov, V. Di Noto, S. McPhail, From Hydrogen Manifesto, through Greebib27n Deal and Just Transition, to Clean Energy Act, Electrochem. Soc. Interface 30 (2021) 57–60, https://doi.org/10.1149/2.F14214IF/XML.
[2] V. Di Noto, H2 in the energy transition, Pure. Appl. Chem. 96 (2024) 451–456, https://doi.org/10.1515/PAC-2023-0707/ASSET/GRAPHIC/J_PAC-2023-0707_FIG_004.JPG.
[3] M. Omrani, M. Goriaux, Y. Liu, S. Martinet, L. Jean-Soro, V. Ruban, Platinum group elements study in automobile catalysts and exhaust gas samples, Environ. Pollut. 257 (2020) 113477, https://doi.org/10.1016/J.ENVPOL.2019.113477.
[4] H.A. Hansen, V. Viswanathan, J.K. Nørskov, Unifying kinetic and thermodynamic analysis of 2 e- and 4 e - reduction of oxygen on metal surfaces, J. Phys. Chem. C 118 (2014) 6706–6718, https://doi.org/10.1021/JP4100608/SUPPL_FILE/JP4100608_SI_001.PDF.
[5] V. Viswanathan, H.A. Hansen, J. Rossmeisl, J.K. Nørskov, Universality in oxygen reduction electrocatalysis on metal surfaces, ACS. Catal 2 (2012) 1654–1660, https://doi.org/10.1021/cs300227s.
[6] N. Alonso-Vante, V. Di Noto, Electrocatalysis for membrane fuel cells: methods, modeling, and applications, Electrocatalysis for membrane fuel cells: methods, Model. Appl. (2023) 1–558, https://doi.org/10.1002/9783527830572.
[7] A. Power, E. Llc, Y. Yang, Direct hydrogen PEM fuel cell powertrain manufacturing cost analysis for heavy duty truck applications. www.AUSTINPOWERENG.com, 2019.
[8] F. Reith, S.G. Campbell, A.S. Ball, A. Pring, G. Southam, Platinum in Earth surface environments, Earth. Sci. Rev 131 (2014) 1–21, https://doi.org/10.1016/J.EARSCIREV.2014.01.003.
[9] C. Fan, K. Quan, Z. Han, F. Han, Z. Li, J. Liu, X. Liu, Recovery and purification of iridium from secondary resources: a review, J. Sustain. Metall. 9 (2023) 909–926, https://doi.org/10.1007/s40831-023-00697-y.
[10] A.J. Appleby, Electrocatalysis and fuel cells, Catal. Rev. 4 (1971) 221–244, https://doi.org/10.1080/01614947108075490.
[11] A. Thakur, P. Thakur, S.M.P. Khurana, Synthesis and applications of nanoparticles, Synthesis and applications of nanoparticles (2022) 1–544. https://doi.org/10.1007/978-981-16-6819-7/COVER.
[12] F.J. Nores-Pondal, I.M.J. Vilella, H. Troiani, M. Granada, S.R. de Miguel, O. A. Scelza, H.R. Corti, Catalytic activity *vs.* size correlation in platinum catalysts of PEM fuel cells prepared on carbon black by different methods, Int. J. Hydrog. Energy 34 (2009) 8193–8203, https://doi.org/10.1016/J.IJHYDENE.2009.07.073.
[13] T. Bauer, K. Singh, G. Mandil, L. Svecova, L. Dubau, Identification of the environmental hotspots of a recycling process - case study of a Pt PEMFC catalyst closed-loop recycling system evaluated via life cycle assessment methodology, Int. J. Hydrog. Energy 63 (2024) 396–410, https://doi.org/10.1016/J.IJHYDENE.2024.03.023.
[14] X. Li, Y. Li, U. Temirov, J. Wang, Z. Chang, Selective recovery of platinum group metals (PGMs) from aqueous solution: advances, challenges, and future perspectives, Sep. Purif. Technol 379 (2025) 134947, https://doi.org/10.1016/J.SEPPUR.2025.134947.
[15] C.H. Chung, S. Cotty, J. Jeon, J. Elbert, X. Su, Auto-oxidation of redox electrodes for the selective recovery of platinum group metals, J. Mater. Chem. Mater 12 (2024) 15006–15018, https://doi.org/10.1039/D4TA01384K.
[16] H. Yildirim, M. Larsen, S.M. Andersen, R. Sharma, S.S. Karade, L.C. Larsen, N. Beyer, Prototype demonstration of innovative and sustainable recycling of materials in polymer electrolyte membrane fuel cells and electrolyzers, ECS. Meet. Abstr. MA2024-02 (2024) 3217, https://doi.org/10.1149/MA2024-02463217MTGABS.
[17] E. Zagoraiou, O. Thoda, E. Polyzou, A.M. Moschovi, I. Yakoumis, Direct reuse of recycled/impure Pt precursor for the production of new electrocatalysts: implementing a sustainable and industrially viable circular hydrogen economy model, Compounds 5 (2025) 32, https://doi.org/10.3390/COMPOUNDS5030032, 2025, Vol. 5, Page 32.
[18] L. Svecova, (Invited) Why and how should the PEMFCs be recycled? – Focus on the MEA case, in: ECS Meeting Abstracts MA2023-02, 2023, p. 1840, https://doi.org/10.1149/MA2023-02381840MTGABS.
[19] M. Kamisono, T. Hanada, M. Goto, Platinum group metal recycling from spent automotive catalysts using reusable hydrophobic deep eutectic solvent, ACS. Sustain. Resour. Manag. 1 (2024) 1021–1028, https://doi.org/10.1021/ACSSUSRESMGT.4C00100.
[20] V.T. Nguyen, S. Riaño, E. Aktan, C. Deferm, J. Fransaer, K. Binnemans, Solvometallurgical recovery of platinum group metals from Spent automotive catalysts, ACS. Sustain. Chem. Eng 9 (2021) 337–350, https://doi.org/10.1021/ACSSUSCHEMENG.0C07355/ASSET/IMAGES/LARGE/SC0C07355_0011.JPEG.
[21] L. Sandig-Predzymirska, T.V. Barreiros, A. Weigelt, S. Pitscheider, C.M. Pedersen, C. Kallesøe, A. Thiere, M. Stelter, A. Charitos, Recovery of platinum and ruthenium from PEM electrodes via hydrometallurgical approach, J. Sustain. Metall. 11 (2025) 145–159, https://doi.org/10.1007/S40831-025-01011-8/FIGURES/12.
[22] T. Hussain, R. Batool, Microemulsion route for the synthesis of nano-structured catalytic materials, in: Properties and Uses of Microemulsions, InTech, 2017, https://doi.org/10.5772/66183.
[23] M. Abe, H. Nishino, K. Ogino, Microemulsion formation with nonionic surfactants-effect of temperature on middle phase Microemulsion formation in nonionic surfactant/alkane/water systems-Masahiko ABE•õ1),•õ2)*, Hiroshi NISHINO•õ1), and Keizo OGINO•õ1),•õ2)*, 1989.
[24] S. Jiang, W. Jiang, J. Wang, Process optimization of simple preparation of AgNPs by polyol method and performance study of a strain sensor, J. Mol. Struct 1292 (2023) 136158, https://doi.org/10.1016/j.molstruc.2023.136158.
[25] D. Larcher, R. Patrice, Preparation of metallic powders and alloys in polyol Media: a thermodynamic approach, J. Solid. State. Chem 154 (2000) 405–411, https://doi.org/10.1006/jssc.2000.8802.
[26] G. Jarvenin. Precipitation and crystallization processes, Alamos National Laboratory, Los, 2009.
[27] M. Berkman, K. Güleç, Pseudo ternary phase diagrams: a practical approach for the area and centroid calculation of stable microemulsion regions, İstanb. J. Pharm. 51 (2021) 42–49, https://doi.org/10.26650/istanbuljpharm.2020.0090.
[28] F. Lorandi, K. Vezzù, A. Nale, G. Pagot, Y.H. Bang, E. Negro, V. Di Noto, Tuning synthesis parameters and support composition for high-performing and durable core-shell Pt–Ni carbon nitride electrocatalysts for the oxygen reduction reaction, J. Power. Sources 555 (2023), https://doi.org/10.1016/j.jpowsour.2022.232390.
[29] L. Lutterotti, About | MAUD - materials analysis using diffraction (and more). https://luttero.github.io/maud/about/, 2000 (accessed July 7, 2025).
[30] D.A. Shirley, High-resolution X-ray photoemission spectrum of the valence bands of gold, Phys. Rev. B 5 (1972) 4709, https://doi.org/10.1103/PhysRevB.5.4709.
[31] E. Negro, A. Nale, K. Vezzù, G. Pagot, S. Polizzi, R. Bertoncello, A. Ansaldo, M. Prato, F. Bonaccorso, I.A. Rutkowska, P.J. Kulesza, V. Di Noto, Hierarchical oxygen reduction reaction electrocatalysts based on FeSn0.5 species embedded in carbon nitride-graphene based supports, Electrochim. Acta 280 (2018) 149–162, https://doi.org/10.1016/J.ELECTACTA.2018.05.126.
[32] S.S. Koche, Y. Garsany, De. Myers, Testing oxygen reduction reaction activity with the rotating disc electrode technique. Http://Energy.Gov/Sites/Prod/Files/2014/03/F12/Webinarslides_rde_technique_031213.Pdf, 2013.
[33] K. Nakamoto, Infrared and raman spectra of inorganic and coordination compounds: part A: theory and applications in inorganic chemistry: sixth edition, Infrared and raman spectra of inorganic and coordination compounds: part A: theory and applications in inorganic chemistry: sixth edition (2008) 1–419. https://doi.org/10.1002/9780470405840.
[34] L.A. Woodward, J.A. Creighton, Raman spectra of the hexachloropalladate, hexachloroplatinate and hexabromoplatinate ions in aqueous solution,

Spectrochim. Acta 17 (1961) 594–599, https://doi.org/10.1016/0371-1951(61)80119-7.
[35] K.V. Yusenko, A.S. Sukhikh, W. Kraus, S.A. Gromilov, Synthesis and crystal chemistry of octahedral rhodium(III) chloroamines, Molecules 25 (2020) 768, https://doi.org/10.3390/MOLECULES25040768, 2020, Vol. 25, Page 768.
[36] B.C. Cornilsen, Solid state vibrational spectra of calcium pyrophosphate dihydrate, J. Mol. Struct 117 (1984) 1–9, https://doi.org/10.1016/0022-2860(84)87237-3.
[37] I.A. Oxton, O. Knop, M. Falk, Infrared spectra of the ammonium ion in crystals. I. Ammonium hexachloroplatinate(IV) and hexachlorotellurate(IV), Can. J. Chem 53 (1975) 2675–2682.
[38] J.D.H. Ana Walt, H.W. Rinn, L.K. Frevel, Chemical analysis by X-ray diffraction: classification and use of X-ray diffraction patterns, Ind. Eng. Chem. -. Anal. Ed. 10 (1938) 457–512, https://doi.org/10.1021/AC50125A001/ASSET/AC50125A001.FP.PNG_V03.
[39] Y. Verde-Gómez, G. Alonso-Nuñez, F. Cervantes, A. Keer, Aqueous solution reaction to synthesize ammonium hexachloroplatinate and its crystallographic and thermogravimetric characterization, Mater. Lett 57 (2003) 4667–4672, https://doi.org/10.1016/S0167-577X(03)00381-1.
[40] P.A. Vaughan, J.H. Sturdivant, L. Pauling, The determination of the structures of complex molecules and ions from X-ray diffraction by their solutions: the structures of the groups PtBr6–, PtCl6–, Nb6Cl12++, Ta6Br12++, and Ta6Cl12++, J. Am. Chem. Soc 72 (1950) 5477–5486, https://doi.org/10.1021/JA01168A028/ASSET/JA01168A028.FP.PNG_V03.
[41] D.R. Lide, CRC Handbook of Chemistry and Physics: A Ready-Reference Book of Chemical and Physical Data, 1995. New York.
[42] M.A. Malik, M.Y. Wani, M.A. Hashim, M.A. Malik, M.Y. Wani, M.A. Hashim, Microemulsion method: a novel route to synthesize organic and inorganic nanomaterials, Arab. J. Chem. 5 (2012) 397–417, https://doi.org/10.1016/J.ARABJC.2010.09.027.
[43] N. Narayan, A. Meiyazhagan, R. Vajtai, Metal nanoparticles as green catalysts, Mater. (Basel) 12 (2019), https://doi.org/10.3390/ma12213602.
[44] M. Brzezińska, E. Szubiakiewicz, M. Jędrzejczyk, Thermal stability of poly(N-vinylpyrrolidone) immobilized on the surface of silica in the presence of noble metals in an atmosphere of hydrogen and oxygen, Mater. Today. Commun 26 (2021) 101706, https://doi.org/10.1016/J.MTCOMM.2020.101706.
[45] P.S. Fernández, D.S. Ferreira, C.A. Martins, H.E. Troiani, G.A. Camara, M. E. Martins, Platinum nanoparticles produced by EG/PVP method: the effect of cleaning on the electro-oxidation of glycerol, Electrochim. Acta 98 (2013) 25–31, https://doi.org/10.1016/J.ELECTACTA.2013.02.129.
[46] S. Karadeniz, N. Ayas, Microwave-assisted synthesis of Pt/C catalyst at high temperatures for PEM fuel cells, Int. J. Hydrog. Energy 52 (2024) 1564–1576, https://doi.org/10.1016/J.IJHYDENE.2023.09.147.
[47] A. Das, N. Yadav, S. Manchala, M. Bungla, A.K. Ganguli, Mechanistic investigations of growth of anisotropic nanostructures in reverse micelles, ACS. Omega 6 (2021) 1007–1029, https://doi.org/10.1021/ACSOMEGA.0C04033/ASSET/IMAGES/MEDIUM/AO0C04033_M001.GIF.
[48] J. Quinson, K.M.Ø. Jensen, From platinum atoms in molecules to colloidal nanoparticles: a review on reduction, nucleation and growth mechanisms, Adv. Colloid. Interface. Sci 286 (2020) 102300, https://doi.org/10.1016/J.CIS.2020.102300.
[49] V. Guterman, K. Paperzh, I. Kantsypa, E. Vetrova, A. Metelitsa, I. Pankov, Y. Pankova, Kinetics of platinum nanoparticles nucleation in polyol synthesis over a wide pH range and properties of Pt/C catalysts, Front. Chem. Sci. Eng. 19 (2025) 1–14, https://doi.org/10.1007/S11705-025-2559-9, 2025 19:6.
[50] H.M. Song, Microemulsion method for the synthesis of Pt/CNTs and Pd/CNTs and their electrocatalytic activities for ethanol oxidation reactions, AIP. Adv 14 (2024), https://doi.org/10.1063/5.0236875/3323948.
[51] T. Hussain, R. Batool, T. Hussain, R. Batool, Microemulsion route for the synthesis of nano-structured catalytic materials, Prop. Uses. Microemulsions (2017), https://doi.org/10.5772/66183.
[52] J. Quinson, Iridium and IrOx nanoparticles: an overview and review of syntheses and applications, Adv. Colloid. Interface. Sci 303 (2022) 102643, https://doi.org/10.1016/J.CIS.2022.102643.
[53] M. Boutonnet, J. Kizling, P. Stenius, G. Maire, The preparation of monodisperse colloidal metal particles from microemulsions, Colloids. Surf. 5 (1982) 209–225, https://doi.org/10.1016/0166-6622(82)80079-6.
[54] M.A. Malik, M.Y. Wani, M.A. Hashim, Microemulsion method: a novel route to synthesize organic and inorganic nanomaterials: 1st Nano update, Arab. J. Chem. 5 (2012) 397–417, https://doi.org/10.1016/J.ARABJC.2010.09.027.
[55] F. Fievet, S. Ammar-Merah, R. Brayner, F. Chau, M. Giraud, F. Mammeri, J. Peron, J.Y. Piquemal, L. Sicard, G. Viau, The polyol process: a unique method for easy access to metal nanoparticles with tailored sizes, shapes and compositions, Chem. Soc. Rev 47 (2018) 5187–5233, https://doi.org/10.1039/C7CS00777A.
[56] R.W.G. Wyckoff, Crystal structures, InterscicencePublischers, 1963.
[57] O. Hassel, Ueber die Kristallstruktur des Graphits, Z. Fuer. Phys. (1924) 317–337.
[58] P. Justin, P.H.K. Charan, G.R. Rao, Activated zirconium carbide promoted Pt/C electrocatalyst for oxygen reduction, Appl. Catal. B 144 (2014) 767–774, https://doi.org/10.1016/J.APCATB.2013.08.024.
[59] Z.N. Zahran, Y. Tsubonouchi, D. Chandra, T. Kanazawa, S. Nozawa, E.A. Mohamed, N. Hoshino, M. Yagi, Extremely efficient and stable hydrogen evolution by a Pt/NiOx composite film deposited on a nickel foam using a mixed metal-imidazole casting method, J. Mater. Chem. Mater 12 (2024) 7094–7106, https://doi.org/10.1039/D3TA06815C.
[60] G. Daniel, Y. Zhang, S. Lanzalaco, F. Brombin, T. Kosmala, G. Granozzi, A. Wang, E. Brillas, I. Sirés, C. Durante, Chitosan-derived nitrogen-doped carbon electrocatalyst for a sustainable upgrade of oxygen reduction to hydrogen peroxide in UV-assisted electro-fenton water treatment, ACS. Sustain. Chem. Eng 8 (2020) 14425–14440, https://doi.org/10.1021/ACSSUSCHEMENG.0C04294/ASSET/IMAGES/LARGE/SC0C04294_0011.JPEG.
[61] A.A. Iurchenkova, E.V. Lobiak, A.A. Kobets, A.N. Kolodin, A. Stott, S.R.P. Silva, E. O. Fedorovskaya, A complex study of the dependence of the reduced graphite oxide electrochemical behavior on the annealing temperature and the type of electrolyte, Electrochim. Acta 370 (2021) 137832, https://doi.org/10.1016/J.ELECTACTA.2021.137832.
[62] S. Diodati, E. Negro, K. Vezzù, V. Di Noto, S. Gross, Oxygen reduction reaction and X-ray photoelectron spectroscopy characterisation of carbon nitride-supported bimetallic electrocatalysts, Electrochim. Acta 215 (2016) 398–409, https://doi.org/10.1016/J.ELECTACTA.2016.08.060.
[63] Z. Wan, Y. Sun, D.C.W. Tsang, I.K.M. Yu, J. Fan, J.H. Clark, Y. Zhou, X. Cao, B. Gao, Y.S. Ok, A sustainable biochar catalyst synergized with copper heteroatoms and CO2 for singlet oxygenation and electron transfer routes, Green. Chem. 21 (2019) 4800–4814, https://doi.org/10.1039/C9GC01843C.
[64] S. Kundu, Y. Wang, W. Xia, M. Muhler, Thermal stability and reducibility of oxygen-containing functional groups on multiwalled carbon nanotube surfaces: a quantitative high-resolution xps and TPD/TPR study, J. Phys. Chem. C 112 (2008) 16869–16878, https://doi.org/10.1021/JP804413A;WGROUP:STRING:ACHS.
[65] P.D. Schulze, S.L. Shaffer, R.L. Hance, D.L. Utley, Adsorption of water on rhenium studied by XPS, J. Vac. Sci. Technol. A 1 (1983) 97–99, https://doi.org/10.1116/1.572321.
[66] R. Sharma, Y. Wang, F. Li, J. Chamier, S.M. Andersen, Synthesis of a Pt/C electrocatalyst from a user-friendly Pt precursor (Ammonium Hexachloroplatinate) through microwave-assisted polyol Synthesis, ACS. Appl. Energy. Mater 2 (2019) 6875–6882, https://doi.org/10.1021/ACSAEM.9B01336/SUPPL_FILE/AE9B01336_SI_001.PDF.
[67] V. Di Noto, E. Negro, Pt-Fe and Pt-Ni carbon nitride-based "core-shell" ORR electrocatalysts for polymer electrolyte membrane fuel cells, Fuel. Cell. 10 (2010) 234–244, https://doi.org/10.1002/FUCE.200900129;WGROUP:STRING:PUBLICATION.
[68] V. Di Noto, E. Negro, B. Patil, F. Lorandi, S. Boudjelida, Y.H. Bang, K. Vezzù, G. Pagot, L. Crociani, A. Nale, Hierarchical metal-[Carbon Nitride Shell/Carbon Core] electrocatalysts: a promising new general approach to tackle the ORR bottleneck in low-temperature fuel cells, ACS. Catal 12 (2022) 12291–12301, https://doi.org/10.1021/ACSCATAL.2C03723/ASSET/IMAGES/LARGE/CS2C03723_0006.JPEG.
[69] V. Di Noto, G. Pagot, E. Negro, K. Vezzù, P.J. Kulesza, I.A. Rutkowska, G. Pace, A formalism to compare electrocatalysts for the oxygen reduction reaction by cyclic voltammetry with the thin-film rotating ring-disk electrode measurements, Curr. Opin. Electrochem 31 (2022) 100839, https://doi.org/10.1016/J.COELEC.2021.100839.